

Experimentally Validated Extended Kalman Filter for UAV State Estimation Using Low-Cost Sensors

S.P.H. Driessen* N.H.J. Janssen* L. Wang** J.L. Palmer***
H. Nijmeijer*

* Eindhoven University of Technology, Den Dolech 2, 5600 MB
Eindhoven, The Netherlands (e-mail: s.p.h.driessen@student.tue.nl)

** RMIT University, 124 La Trobe Street, Melbourne VIC 3000,
Australia (e-mail: liuping.wang@rmit.edu.au)

*** DST Group, 506 Lorimer Street, Port Melbourne VIC 3207,
Australia (e-mail: jennifer.palmer@dst.defence.gov.au)

Abstract: Visually based velocity and position estimations are often used to reduce or remove the dependency of an unmanned aerial vehicle (UAV) on global navigation satellite system signals, which may be unreliable in urban canyons and are unavailable indoors. In this paper, a sensor-fusion algorithm based on an extended Kalman filter is developed for the velocity, position, and attitude estimation of a UAV using low-cost sensors. In particular an inertial measurement unit (IMU) and an optical-flow sensor that includes a sonar module and an additional gyroscope are used. The algorithm is shown experimentally to be able to handle measurements with different sampling rates and missing data, caused by the indoor, low-light conditions. State estimations are compared to a ground-truth pose history obtained with a motion-capture system to show the influence of the optical-flow and sonar measurements on its performance. Additionally, the experimental results demonstrate that the velocity and attitude can be estimated without drift, despite the magnetic distortions typical of indoor environments.

© 2018, IFAC (International Federation of Automatic Control) Hosting by Elsevier Ltd. All rights reserved.

Keywords: Unmanned aerial vehicle, Sensor fusion, Extended Kalman filter, Optical flow, Visual-inertial state estimation, Missing data, Multi-rate sampled data.

1. INTRODUCTION

Unmanned aerial vehicles (UAVs) can be used for a wide range of applications, such as rescue (Pólka et al., 2017) (Waharte and Trigoni, 2010), visual inspection (Omari et al., 2015) and manufacturing (Khosiawan and Nielsen, 2016). Knowledge of the UAV's velocity, position, and attitude is essential in these applications. On-board sensors generally are required to be inexpensive, compact, light, and low-powered. An inertial measurement unit (IMU) satisfies these requirements and allows for tri-axial measurement of the acceleration and angular velocity. Often the IMU also features a magnetometer. As a result of sensor noise and a slowly varying sensor bias, combined with vibrations generated by the UAV's motors, direct integration of acceleration and angular velocity leads to poor velocity and attitude estimations that tend to drift over time. Sensor fusion can greatly increase the estimation performance. In this context accelerometer and magnetometer measurements can be combined to retrieve attitude information. For translational velocity and position, global navigation satellite system (GNSS) signals can provide a reference. However, GNSS signals are not always reliable and are typically unavailable indoors.

Recently developed camera-based vision sensors are light and inexpensive and can also be used to estimate velocity (Mebarki et al., 2013) and position (Weiss and Sieg-

wart, 2011). Within these sensors, sequential images are used to calculate the optical flow. To relate optical-flow measurements to the camera's translational velocity, the scene depth must be known. It may be measured directly using, for example, sonar or LiDAR sensors or estimated using sensor fusion. The latter approach is taken in Bleser and Hendebey (2010), where an optical-flow-based extended Kalman filter (EKF) is developed and validated through simulation. A real-time implementation of an optical-flow-based EKF with a similar approach can be found in Weiss et al. (2012). LiDAR measurements are used in, for example, Yun et al. (2016) and Goppert et al. (2017).

In this paper, the low-cost PX4Flow optical-flow sensor (OFS) is used. This is an open-source based software and hardware platform that uses a CMOS vision sensor, a gyroscope, and a sonar range finder (Honegger et al., 2013). The sonar module can be replaced with a LiDAR sensor to increase the data output rate and measurement quality. However, LiDAR sensors are considerably more expensive. Therefore a different approach is taken in this paper. Sonar measurements are not used directly to scale the flow velocity to the camera's translational velocity, instead a state representing the UAV height, which is updated with sonar and IMU measurements, is used. This results in a more robust translational-velocity estimate. An EKF-based framework, modified to handle multi-rate sampled measurements and missing data, is used to perform

this update and to estimate the UAV's velocity, position, and attitude. The resulting fusion algorithm is validated experimentally.

2. SENSORS MODELS

2.1 Notation

For simplicity, the IMU and OFS are assumed to be aligned and to produce measurements with respect to the same right-handed body frame, which is attached to the UAV. The right-handed world frame is fixed to the Earth, with the x -axis aligned with the local magnetic north and the z -axis pointing opposite to gravity. Superscripts b and w are used to indicate that a variable is expressed in the body or the world frame, respectively; while subscripts x , y , and z refer to the component of a variable along each axis. The rotation matrix, representing the rotation of the world frame with respect to the body frame, is denoted as $R(\Phi^w)_w^b$, with attitude $\Phi^w = [\phi \ \theta \ \psi]^T$, where ϕ , θ , and ψ are the roll, pitch, and yaw of the UAV, respectively, measured with respect to the x -, y -, and z -axes of the world frame. To transform the angular velocity from the world to body frame, the matrix $T(\Phi^w)_w^b$ is used. However, if the IMU and OFS measure in different frames, due to, for example, misalignment, the EKF can be adapted to account for the difference in their reference frames. Even if the relative position and rotation are not known, the EKF can be used to estimate those quantities (Weiss and Siegwart, 2011).

2.2 Sensor equations

The accelerometer, magnetometer, and gyroscopes measure in three perpendicular directions. These measurements are modelled with bias and noise terms, b and μ , respectively, which yields (Sabatini, 2011):

$$\begin{aligned}\tilde{a}^b &= R_w^b(\Phi^w)(a^w + g^w) + b_a + \mu_a, \\ \tilde{\omega}_I^b &= T_w^b(\Phi^w)\omega^w + b_{\omega_I} + \mu_{\omega_I}, \\ \tilde{m}^b &= R_w^b(\Phi^w)m^w + b_m + \mu_m, \\ \tilde{\omega}_O^b &= T_w^b(\Phi^w)\omega^w + b_{\omega_O} + \mu_{\omega_O},\end{aligned}\quad (1)$$

where a tilde (\sim) indicates the measurement under consideration. Variables $a = [a_x \ a_y \ a_z]^T$, $\omega = [\omega_x \ \omega_y \ \omega_z]^T$, and $m = [m_x \ m_y \ m_z]^T$ represent the acceleration (m/s^2), angular velocity (rad/s), and magnetic field (μT), respectively. Subscripts I and O distinguish between the angular velocity measured by the IMU and that from the OFS, respectively. The world's gravitational vector is given by $g^w = [0 \ 0 \ 9.81]^T$ (m/s^2). Scale factors are omitted (i.e., chosen to be equal to 1), as they have a limited influence compared to the bias drifts in these sensors (Sabatini, 2011).

The OFS measures the optical flow, ρ (pixel), in the x - and y -directions of the body frame, between two consecutive images. This flow is induced by the translational and angular velocities of the UAV, $v = [v_x \ v_y \ v_z]^T$ (m/s) and ω , respectively (Honegger et al., 2013). To relate the optical flow to the UAV's velocity, the time between two consecutive images, τ (s), and focal length of the sensor's optics, f (pixel), are needed. Furthermore, the

scene depth is needed. It is related to the UAV's position, $p = [p_x \ p_y \ p_z]^T$ (m), in the z -direction along with the roll and pitch angles. The sonar measures the scene depth, s_z^b (m). The optical flow and scene depth can be expressed as

$$\begin{aligned}\tilde{\rho}_x^b &= -\left(\frac{\cos(\phi)\cos(\theta)v_x^b}{p_z^w} + \omega_y^b\right)\tau f + \mu_{\rho_x}, \\ \tilde{\rho}_y^b &= -\left(\frac{\cos(\phi)\cos(\theta)v_y^b}{p_z^w} + \omega_x^b\right)\tau f + \mu_{\rho_y}, \\ \tilde{s}_z^b &= \frac{p_z^w}{\cos(\phi)\cos(\theta)} + \mu_{s_z}.\end{aligned}\quad (2)$$

Noise terms are modelled as $\mu_i \sim \mathcal{N}(0, \Sigma_i)$, with $i \in \{a, \omega_I, m, \rho_x, \rho_y, s_z, \omega_O\}$ and Σ_i diagonal, where $\mathcal{N}(0, \Sigma_i)$ denotes a normal (Gaussian) distribution with a zero mean and a covariance of Σ_i . Bias terms are often modelled independently, following a random-walk process (Sabatini, 2011):

$$\dot{b}_j = \mu_{b_j}, \quad j \in \{a, \omega_I, m, \omega_O\}, \quad (3)$$

with $\mu_{b_j} \sim \mathcal{N}(0, \Sigma_{b_j})$ and Σ_{b_j} diagonal. Because magnetometer bias drift is usually negligible, b_m is primarily used to compensate for magnetic distortions. Note that variables v and ω in the model for the pixel flow are expressed in the body frame. Transformation to the world frame can be done using the rotation matrices.

3. SENSOR-FUSION ALGORITHM

An EKF is used to estimate the UAV's position, attitude, and velocity. Therefore, the state vector is defined as

$$\zeta = [(p^w)^T \ (v^w)^T \ (\Phi^w)^T \ (\omega^w)^T \ b_a^T \ b_{\omega_I}^T \ b_{\omega_O}^T \ b_m^T]^T. \quad (4)$$

The biases in the sensors are included in the state space, so they can be estimated by the EKF algorithm, which consists of multiple steps.

3.1 Prediction step

An *a-priori* state prediction is made using a discrete-time process model with time step, t (s). The accelerometer and gyroscope from the IMU are used to define the input as $u^T = [\tilde{a}^T \ \tilde{\omega}_I^T]$. This allows for a state vector without acceleration states and therefore reduces its size. Fewer noise covariances must be estimated, which simplifies the tuning of the EKF. Furthermore it saves one measurement update, which reduces the size of the matrix inversions (Bleser and Stricker, 2009). Rewriting (1) and (3), the discrete equations governing the state are obtained:

$$\begin{aligned}p_{k+1}^w &= p_k^w + t v_k^w, \\ v_{k+1}^w &= v_k^w + t[R_b^w(\Phi_k^w)(\tilde{a}^b - b_{a,k} - \mu_a) - g^w], \\ \Phi_{k+1}^w &= \Phi_k^w + t \omega_k^w, \\ \omega_{k+1}^w &= T_b^w(\Phi_k^w)(\tilde{\omega}_I^b - b_{\omega_I,k} - \mu_{\omega_I}), \\ b_{a,k+1} &= b_{a,k} + t \mu_{b_{a,k}}, \\ b_{\omega_I,k+1} &= b_{\omega_I,k} + t \mu_{b_{\omega_I,k}}, \\ b_{\omega_O,k+1} &= b_{\omega_O,k} + t \mu_{b_{\omega_O,k}}, \\ b_{m,k+1} &= b_{m,k} + t \mu_{b_{m,k}};\end{aligned}\quad (5)$$

or, in short,

$$\zeta_{k+1} = f(\zeta_k, u_k, w_k). \quad (6)$$

The process noise, $w_k \sim \mathcal{N}(0, Q)$, where Q is the covariance matrix, given by $w_k^T = [\mu_a^T \mu_{\omega_I}^T \mu_{b_a}^T \mu_{b_{\omega_I}}^T \mu_{b_{\omega_O}}^T \mu_{b_{sz}}^T]$, is set to zero in the prediction because it is unknown. This results in the *a-priori* state prediction:

$$\hat{\zeta}_{k+1}^- = f(\hat{\zeta}_k, u_k, 0), \quad (7)$$

where the caret (^) denotes that the variable is estimated and the superscript “-” denotes a prediction. The *a-priori* covariance matrix estimation is defined as

$$P_{k+1}^- = F_k P_k F_k^T + W_k Q W_k^T, \quad (8)$$

where the matrices F_k and W_k are given by

$$F_k = \frac{\partial f}{\partial \zeta}(\hat{\zeta}_k, u_k, 0), \quad (9)$$

$$W_k = \frac{\partial f}{\partial w}(\hat{\zeta}_k, u_k, 0). \quad (10)$$

3.2 Measurement model

Data from the IMU and the gyroscope included in the OFS are assumed to have the same sampling rate and to be available at each time step. The corresponding measurement model is taken as:

$$\eta_{\text{IMU},k} = \begin{bmatrix} R_w^b(\hat{\Phi}_k^w)g^w + \hat{b}_{a,k} + \mu_{a,k} \\ R_w^b(\hat{\Phi}_k^w)m^w + \hat{b}_{m,k} + \mu_{\omega_I,k} \\ T_w^b(\hat{\Phi}_k^w)\hat{\omega}_k^w + \hat{b}_{\omega_I,k} + \mu_{\omega_I,k} \\ T_w^b(\hat{\Phi}_k^w)\hat{\omega}_k^w + \hat{b}_{\omega_O,k} + \mu_{\omega_O,k} \end{bmatrix}. \quad (11)$$

Note that the first line in (11) assumes that the linear accelerations are small compared to the gravitational acceleration (Strohmeier and Montenegro, 2017). The measurement models for the sonar and optical-flow measurements are, in correspondence with (2), given by

$$\eta_{\text{sonar},k} = \frac{\hat{p}_z^w}{\cos(\hat{\phi}) \cos(\hat{\theta})} + \mu_{sz}, \quad (12)$$

$$\eta_{\text{OFS},k} = \begin{bmatrix} - \left(\frac{\cos(\hat{\phi}) \cos(\hat{\theta}) \hat{v}_{x,k}^b}{\hat{p}_{z,k}^w} + \hat{\omega}_{y,k}^b \right) \tau_k f + \mu_{px} \\ - \left(\frac{\cos(\hat{\phi}) \cos(\hat{\theta}) \hat{v}_{y,k}^b}{\hat{p}_{z,k}^w} + \hat{\omega}_{x,k}^b \right) \tau_k f + \mu_{py} \end{bmatrix}. \quad (13)$$

The OFS does not output new flow data at a constant rate due to its automatic exposure control (AEC). The flow quality, $\alpha \in [0, 255]$, is an output of the PX4Flow that depends on the number of pixels that match in two consecutive images. Sometimes this flow-data quality is equal to $\alpha = 0$ due to, e.g., poor lighting conditions from which no flow could be calculated. Because not all sensors generate a usable output at every time step, the variables $\beta \in \{0, 1\}$ and $\gamma \in \{0, 1\}$ are introduced. If new flow values have become available since the last time step and the corresponding quality is larger than zero, β equals 1. If new sonar information has become available, γ equals 1. Otherwise both variables equal zero.

Four measurement models can be distinguished:

$$\eta_k = \begin{cases} \eta_{\text{IMU},k}, & \text{if } \beta = 0 \wedge \gamma = 0, \\ \begin{bmatrix} \eta_{\text{OFS},k} \\ \eta_{\text{IMU},k} \end{bmatrix}, & \text{if } \beta = 1 \wedge \gamma = 0, \\ \begin{bmatrix} \eta_{\text{sonar},k} \\ \eta_{\text{OFS},k} \\ \eta_{\text{IMU},k} \end{bmatrix}, & \text{if } \beta = 1 \wedge \gamma = 1, \\ \begin{bmatrix} \eta_{\text{sonar},k} \\ \eta_{\text{IMU},k} \end{bmatrix}, & \text{if } \beta = 0 \wedge \gamma = 1; \end{cases} \quad (14)$$

or, in short,

$$\eta_k = h(\hat{\zeta}_k^-, \nu_k), \quad (15)$$

where $\nu \sim \mathcal{N}(0, R)$ defines the zero-mean Gaussian measurement noise and R is the noise covariance matrix.

3.3 Kalman gain

The Kalman gain, K , is computed using

$$K_{k+1} = P_{k+1}^- H_{k+1}^T (H_{k+1} P_{k+1}^- H_{k+1}^T + V_{k+1} R V_{k+1}^T)^{-1}, \quad (16)$$

where the matrix H_{k+1} is defined as

$$H_{k+1} = \frac{\partial h}{\partial \zeta}(\hat{\zeta}_{k+1}^-, 0) \quad (17)$$

and the matrix V_{k+1} is defined as

$$V_{k+1} = \frac{\partial h}{\partial \nu}(\hat{\zeta}_{k+1}^-, 0) = I, \quad (18)$$

where I is the identity matrix.

3.4 Correction step

Similar to the measurement model, the measurement matrix also varies with time. The IMU and gyroscope of the OFS have new measurements at each time step, with the corresponding matrix:

$$\tilde{\eta}_{\text{IMU},k} = \begin{bmatrix} \tilde{a}_k^b \\ \tilde{m}_k^b \\ \tilde{\omega}_{I,k}^b \\ \tilde{\omega}_{O,k}^b \end{bmatrix}. \quad (19)$$

A new OFS measurement results in two flow values:

$$\tilde{\eta}_{\text{OFS},k} = \begin{bmatrix} \tilde{\rho}_{x,k}^b \\ \tilde{\rho}_{y,k}^b \end{bmatrix}, \quad (20)$$

while the measurement vector of the sonar is given by

$$\tilde{\eta}_{\text{sonar},k} = \tilde{s}_{z,k}^b. \quad (21)$$

Because there are multiple possibilities at each time step, the total measurement vector is defined as

$$\tilde{\eta}_k = \begin{cases} \tilde{\eta}_{\text{IMU},k}, & \text{if } \beta = 0 \wedge \gamma = 0, \\ \begin{bmatrix} \tilde{\eta}_{\text{OFS},k} \\ \tilde{\eta}_{\text{IMU},k} \end{bmatrix}, & \text{if } \beta = 1 \wedge \gamma = 0, \\ \begin{bmatrix} \tilde{\eta}_{\text{sonar},k} \\ \tilde{\eta}_{\text{OFS},k} \\ \tilde{\eta}_{\text{IMU},k} \end{bmatrix}, & \text{if } \beta = 1 \wedge \gamma = 1, \\ \begin{bmatrix} \tilde{\eta}_{\text{sonar},k} \\ \tilde{\eta}_{\text{IMU},k} \end{bmatrix}, & \text{if } \beta = 0 \wedge \gamma = 1. \end{cases} \quad (22)$$

The corrected state vector and covariance matrix can now be calculated as

$$\hat{\zeta}_{k+1} = \hat{\zeta}_{k+1}^- + K_{k+1} (\tilde{\eta}_{k+1} - \eta_{k+1}(\zeta_{k+1}^-, 0)) \quad \text{and} \quad (23)$$

$$P_{k+1} = (I - K_{k+1} H_{k+1}) P_{k+1}^-. \quad (24)$$

4. EXPERIMENTAL VALIDATION

Experiments are carried out to validate and tune the EKF.

4.1 Experimental setup

A stand-alone sensor module featuring a PX4Flow, an Adafruit Precision NXP 9-DOF Breakout Board, and a Teensy 3.6 development board is attached to a hexacopter with a 3DR Pixhawk flight controller. All sensors are calibrated prior to the experiments. A photograph of the hexacopter is shown in Fig 1.

The UAV is flown under manual remote control in an indoor flight laboratory, while sensor outputs are written to a micro-SD card by the Teensy board. The flight time and therefore the measurement duration is limited by battery capacity to approximately 150 s. This dataset is post-processed by the EKF. The position and attitude used as ground truth are measured by an OptiTrack motion-capture system, which yields positional and attitudinal data with uncertainties of <1 mm and <0.02 rad, respectively. The angular and translational velocities are obtained by differentiation.

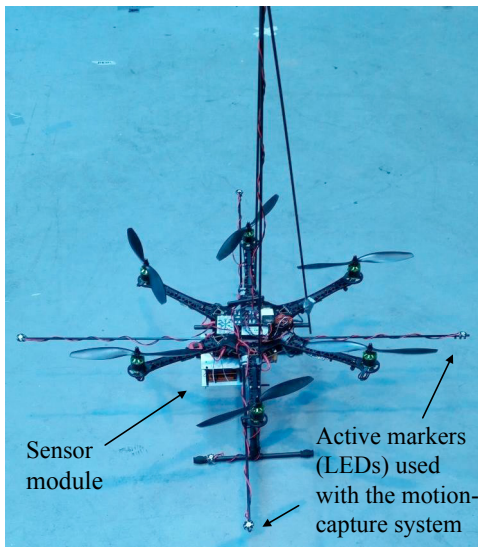


Fig. 1. UAV with sensor module attached

As described in Section 3.2, flow data is recorded with a variable frequency due to the AEC. Thus, the firmware of the PX4Flow is altered so that the time between the two images used for the optical-flow calculation is also recorded, for use in (13). Furthermore, the built-in bias correction of the gyroscope is turned off, as the correction has been taken into account in the EKF. The sampling rate of the gyroscope of the PX4Flow and the IMU is chosen to be 200 Hz. The sonar sensor has a range of 0.3–5 m, and its measurements are limited to a sampling rate of ~10 Hz.

The initial states are estimated by leaving the UAV on the ground for a period of time. This automatically implies the initial states, $v_0 = 0$ and $\omega_0 = 0$. The positions, $p_{x,0}$ and $p_{y,0}$, are chosen to be zero; and the initial vertical position, $p_{z,0}$, is the measured distance from the sonar to the ground. The initial attitude of the UAV is calculated using (Munguia and Grau, 2011)

$$\begin{aligned} \phi_0 &= \arctan \left(\frac{\bar{a}_y^b}{\bar{a}_z^b} \right), \\ \theta_0 &= \arctan \left(-\frac{\bar{a}_x^b}{\bar{a}_y^b s(\phi_0) + \bar{a}_z^b c(\phi_0)} \right), \\ \psi_0 &= \arctan \left(\frac{-\bar{m}_y^b c(\phi_0) + \bar{m}_z^b s(\phi_0)}{\bar{m}_x^b c(\theta_0) + \bar{m}_y^b s(\phi_0) s(\theta_0) + \bar{m}_z^b c(\phi_0) s(\theta_0)} \right), \end{aligned} \quad (25)$$

where \bar{a} and \bar{m} are the average acceleration and magnetic field measured during the initialisation period and $c(\cdot) = \cos(\cdot)$ and $s(\cdot) = \sin(\cdot)$. To derive estimates of the covariance matrices Q and R , the UAV's motors are turned on while the UAV remains on a level surface. During this experiment the UAV does not move, yet vibrations and disturbances also present during flight, are introduced. All accelerations other than that due to gravity are zero, because the UAV is not moving. The standard deviations of the values obtained from these measurements are used to estimate Q and R .

The magnetic field in the experimental environment is not constant during flight due to the metallic structure of the laboratory, which causes bad magnetometer measurements. Therefore the covariance of the magnetometer bias is set to a large value to compensate.

4.2 Results

The gathered dataset is fused in post-processing using the described EKF and the state estimates are compared to the motion-capture results. The first 40 s of the measurement are used for sensor calibration and are not taken into account otherwise. The EKF and motion-capture datasets are synchronised by hand using data collected during the calibration period. The attitude estimation is shown in Fig. 2, where it can be seen to be estimated without drift. The magnetometer bias (not shown) has the same trends as the position of the UAV and is able to compensate for position-dependent magnetic distortions.

In Fig. 3, the translational-velocity estimates are shown, along with the flow quality. Between 40 and 53 s, reliable flow values are unavailable, which means that the velocity is estimated by integrating the accelerometer data. This clearly leads to errors in the horizontal translational-

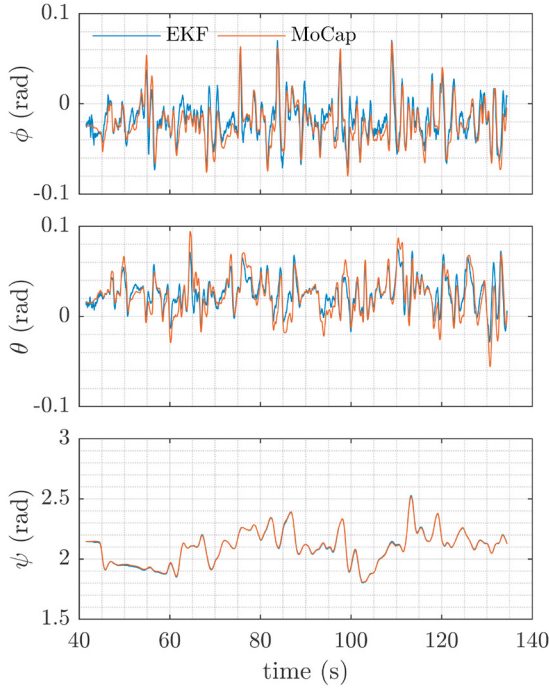


Fig. 2. Estimated attitude compared to ground truth

velocity estimates. When the OFS supplies reliable data, this error is corrected. The OFS improves the velocity estimate and compensates for the drift that is normally present as a result of integrating the IMU data. As long as the OFS outputs data with a sufficiently high rate and quality, the velocity error remains relatively low.

The results for the position estimate are shown in Fig. 4. Drift as a result of the bad flow quality at 40–50 s is clearly visible in the y -position. When the flow data are available, the drift becomes significantly smaller. Drift in the z -direction also occurs during the first few seconds, when the actual height of the UAV is less than 0.3 m and thus not within the range of the sonar. As soon as the UAV's height is within the sonar range, the position estimate in z -direction is corrected and drift does not occur. The other two components of position do not have absolute measurements, and drift can therefore not be entirely prevented.

Table 1 summarises the estimation results in terms of root-mean-squared error (RMSE) values. The second column represents the RMSE of the state estimates using all sensor measurements in the EKF. These values correspond to the estimates shown in Figs. 2, 3, and 4. The third column represents a case when the optical-flow measurements are not used. The main difference is the RMSE of v_x and v_y , which create poor estimates for p_x and p_y . The vertical velocity estimate (v_z) has RMSE values similar to those in column two, because the estimate is independent of the flow data. Furthermore, the influence on the attitude estimation is negligible. The fourth column represents the RMSE values when the sonar measurements are neglected and shows that the error in p_z has increased significantly. Because p_z is also used to scale flow data, all velocity estimates have higher RMSE values. Also the yaw error increases significantly, while other estimates do not show

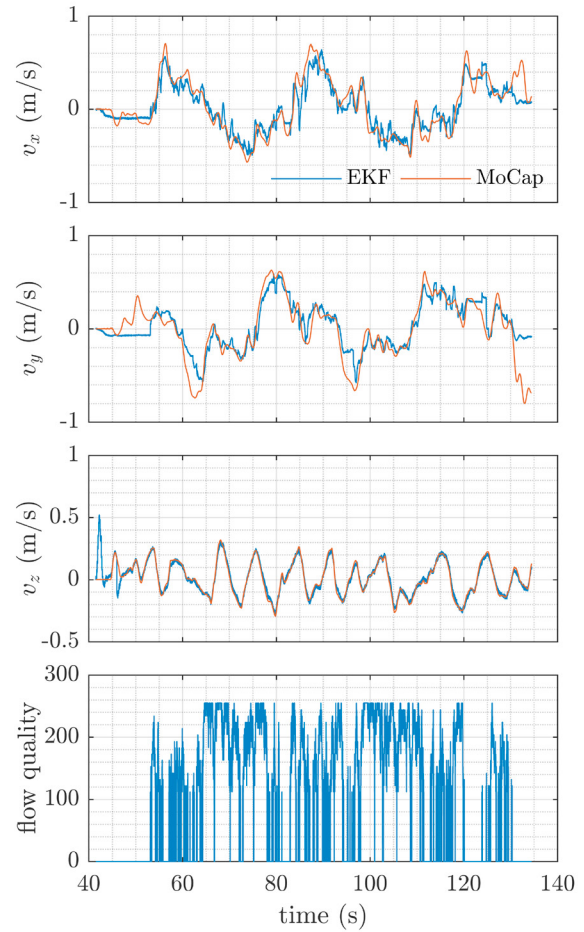


Fig. 3. Estimated velocity compared to ground truth

large differences. When neither flow nor the sonar data are used, state estimates have the RMSE values shown in column five. The effects described earlier are visible, but the yaw error does not increase as much as when the sonar sensor data alone are omitted. This is caused by the bad scaling of the flow data, due to a lack of an adequate range measurement, which corrupts the yaw estimate.

To validate that the EKF also performs well with different datasets and that the matrices Q and R do not have to be adapted to obtain good estimates, the unaltered fusion algorithm is used on measurement data from another flight. The RMSE of the resulting estimates are given in the last column of Table 1. For this estimate, all available measurements were used. It can be seen that for this dataset, the EKF provides similar results to those shown in the first column.

4.3 Discussion

During the experiments, the PX4Flow sensor is found to be very sensitive to the lighting conditions and ground surface. Measurements taken outside, on an asphalt surface, result in high-quality flow data without gaps. The indoor measurements are performed on a smooth, concrete surface, resulting in the flow quality shown in Fig. 3, in which gaps are clearly visible. Fast movements in low-

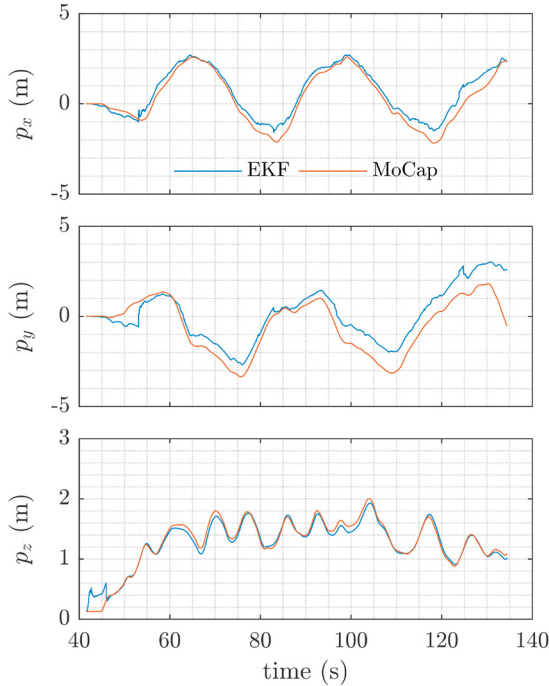


Fig. 4. Estimated position compared to ground truth

Table 1. RMSE values for different cases

	Ref.	No flow	No sonar	No flow, no sonar	2nd dataset
e_{p_x} (m)	0.4281	13.5987	1.3174	13.3775	0.7826
e_{p_y} (m)	0.8573	3.7590	1.6040	3.6392	1.0779
e_{p_z} (m)	0.0782	0.0783	1.3594	3.9486	0.0810
e_{v_x} (m/s)	0.1150	0.4850	0.3075	0.4846	0.1054
e_{v_y} (m/s)	0.1666	0.3166	0.3407	0.3161	0.1224
e_{v_z} (m/s)	0.0461	0.0461	0.1341	0.1361	0.0486
e_ϕ (rad)	0.0118	0.0125	0.0138	0.0125	0.0115
e_θ (rad)	0.0116	0.0131	0.0139	0.0131	0.0135
e_ψ (rad)	0.0051	0.0074	0.0283	0.0074	0.0067
$e_{\dot{\phi}}$ (rad/s)	0.0431	0.0450	0.0426	0.0450	0.0399
$e_{\dot{\theta}}$ (rad/s)	0.0266	0.0264	0.0267	0.0264	0.0306
$e_{\dot{\psi}}$ (rad/s)	0.0176	0.0176	0.0176	0.0176	0.0186

lighting conditions also resulted in low-quality flow data.

Sonar measurements are greatly affected by the ground surface: a smooth hard surface gives good quality height measurements, compared to a softer and rougher surface.

5. CONCLUSIONS

In this paper, an EKF is proposed to fuse sensor data from an IMU, an OFS, and a sonar sensor. Bias compensation is used to correct for drift in these sensors. The EKF is validated by comparing the state estimates to the ground truth provided by a motion-capture system. The experimental results indicate the translational velocity of the UAV, as well as its attitude and angular velocity, may be estimated without drift. The availability of flow data greatly reduces the error in velocity and position in the $x - y$ plane. Sonar measurements result in better estimation of the velocity and position in the z -direction. The sonar and optical-flow measurements do not significantly influence the attitude estimates. Future extensions can be

made by implementing the algorithm on-board the UAV and inputting estimates from the EKF output to a flight controller.

REFERENCES

- Bleser, G. and Hendeb, G. (2010). Using optical flow for filling the gaps in visual-inertial tracking. *European Signal Processing Conference*, 1836–1840.
- Bleser, G. and Stricker, D. (2009). Advanced tracking through efficient image processing and visual-inertial sensor fusion. *Computers and Graphics*, 33(1), 59–72.
- Goppert, J., Yantek, S., and Hwang, I. (2017). Invariant Kalman filter application to optical flow based visual odometry for UAVs. *Ninth International Conference on Ubiquitous and Future Networks*, 99–104.
- Honegger, D., Meier, L., Tanskanen, P., Pollefeys, M., and Eth, Z. (2013). An open source and open hardware embedded metric optical flow CMOS camera for indoor and outdoor applications. *IEEE International Conference on Robotics and Automation*, 1736–1741.
- Khosiawan, Y. and Nielsen, I. (2016). A system of UAV application in indoor environment. *Production and Manufacturing Research*, 4(1), 2–22.
- Mebarki, R., Cacace, J., and Lippiello, V. (2013). Velocity estimation of an UAV using visual and IMU data in a GPS-denied environment. *IEEE International Symposium on Safety, Security, and Rescue Robotics*.
- Munguia, R. and Grau, A. (2011). Attitude and heading system based on EKF total state configuration. *Proceedings of the 2011 IEEE International Symposium on Industrial Electronics*, 2147–2152.
- Omari, S., Gohl, P., Burri, M., Achtelek, M., and Siegwart, R. (2015). Visual industrial inspection using aerial robots. *Proceedings of the 3rd International Conference on Applied Robotics for the Power Industry*, (1).
- Pólka, M., Ptak, S., and Kuziora, L. (2017). The use of UAV's for search and rescue operations. *Procedia Engineering*, 192, 748–752.
- Sabatini, A.M. (2011). Kalman-filter-based orientation determination using inertial/magnetic sensors: Observability analysis and performance evaluation. *Sensors*, 11(10), 9182–9206.
- Strohmeier, M. and Montenegro, S. (2017). Coupled GPS/MEMS IMU attitude determination of small UAVs with COTS. *Electronics*, 6(1), 15.
- Waharte, S. and Trigoni, N. (2010). Supporting search and rescue operations with UAVs. *International Conference on Emerging Security Technologies (ETS)*, 142–147.
- Weiss, S., Achtelek, M.W., Lynen, S., Chli, M., and Siegwart, R. (2012). Real-time onboard visual-inertial state estimation and self-calibration of MAVs in unknown environments. *IEEE International Conference on Robotics and Automation*, 957–964.
- Weiss, S. and Siegwart, R. (2011). Real-time metric state estimation for modular vision-inertial systems. *Proceedings of the IEEE International Conference on Robotics and Automation*, 231855, 4531–4537.
- Yun, S., Lee, Y.J., and Sung, S. (2016). Range/optical flow-aided integrated navigation system in a strapdown sensor configuration. *International Journal of Control, Automation and Systems*, 14(1), 229–241.